Multidimensional Simulation and Optimization of Hybrid Laser and Discharge Plasma Devices for EUV Lithography

A. Hassanein*, V. Sizyuk, and T. Sizyuk
Purdue University, West Lafayette, IN, USA 47907

ABSTRACT

Current devices for EUV lithography combine both laser and discharge physics to achieve sufficient brightness with minimum debris generation to support the throughput requirements of High-Volume Manufacturing (HVM) lithography exposure tools with long lifetime. Source performance, Debris mitigation, and reflector system are critical to efficient EUV collection and component lifetime. Integrated models are developed to simulate EUV emission at high power and debris generation and transport in hybrid EUV devices. The models being developed include, for example, new ideas and parameters of laser beams in discharge devices. In addition, optimization of source parameters, combination magnetic fields and gas jet parameters to significantly reduce the debris, and mirror surface conditions to enhance the reflectivity of EUV. Source optimization studies include full 3-D simulation of laser interaction with tin targets followed by discharge simulation to produce the optimum EUV photons. Initial simulations show that for HVM devices a combination of source optimization, innovative debris mitigation system, and understanding debris/mirror interaction is required to achieve the lifetime needed.

Keywords: EUV devices, LPP, DPP, HEIGHTS, Debris mitigation, MHD, Gaseous jets, Collection mirrors.

1. INTRODUCTION

The EUV radiation can be generated by several methods: discharge-produced plasma (DPP), laser-produced plasma (LPP), and synchrotron radiation. Each method has advantages and disadvantages. In order to meet the requirements of the Intel Lithography Roadmap goals for high-volume manufacturing [1] and SEMATECH's EUV Source Program goal [2], the EUV source is required to have power exceeding 200 W at a wavelength of 13.5 nm (2% bandwidth). Various LPP and gas DPP devices are under development and investigation [3]-[7]. At present, several of the EUV sources begin to realize the power level demanded by commercial chip manufacturers. The conversion efficiency (CE) of the EUV radiation is an important factor in the successful development of the source. Many additional factors are also important and influence the efficiency of the EUV device, such as the plasma material, form and size of the radiated area, collectable solid angle, and the amount of debris generated. It is best to use the CE for optimal operating condition to get a realistic utility consumption estimate and understand the limits of power scaling. For the LPP system, the laser power and EUV output in the 2% bandwidth around 13.5 nm is used to estimate the CE. However, for LPP systems, the overall conversion for the entire system is much less than for DPP because of the low wall-plug-to-laser-light CE of a laser system, which is typically less than 10% [2]. In this situation where competition between the laser and discharge devices remains, the hybrid LPP+DPP systems (Fig.1.) can give new pulse for the development of new most effective EUV sources for the lithography. The first attempts to combine the plasma preparation with laser and subsequent discharge compression for the EUV lithography purpose were carried out lately [8]-[10]. The progress in developing the hybrid devices is at the early phases.

Because many physical processes are involved, and many technical problems need to be solved when developing and optimizing a particular EUV device, laboratory experiments would be very expensive and may be impossible; therefore, only computer modeling can generate a complete picture of EUV devices within a reasonable time and at a reasonable cost. Ideally, an integrated physical model should be developed specifically for simulating plasma behavior in both DPP and LPP devices. The model should include atomic physics, hydrodynamics, plasma heat conduction, and photon radiation transport. The EUV source should be modeled completely: from the energy input mechanism and plasma formation, up to EUV output from the pinch or laser target and the mirror collector system.

*hassanein@purdue.edu; phone 1 765 496-9731; fax 1 765 496-2233

Emerging Lithographic Technologies XII, edited by Frank M. Schellenberg
Proc. of SPIE Vol. 6921, 692113, (2008) · 0277-786X/08/$18 · doi: 10.1117/12.771218

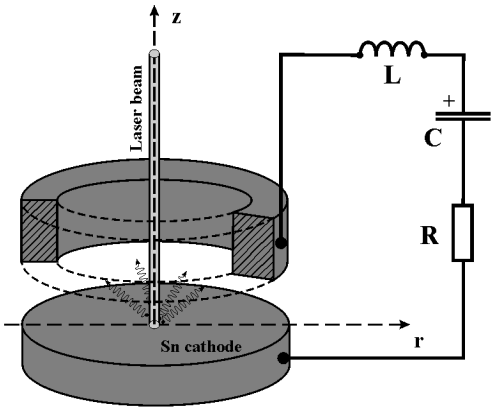

Fig. 1. Schematic illustration of DPP+LPP hybrid device.

Each physical process should be described adequately, and each physical problem should be solved using the most advanced numerical scheme to enhance accuracy and to reduce computational time. The radiation conditions at the intermediate focus of a manufacturers EUVL stepper can then be predicted most accurately. Our previous progress in modeling of the plasma devices shows real capabilities of the integrated theoretical model developments [11]-[15]. Based on the developed physical and mathematical model, our High Energy Interaction with Heterogeneous Target Systems (HEIGHTS) computer package allows to simulate the full cycle of plasma evolution in LPP or/and DPP devices.

2. MATHEMATICAL MODEL

2.1 Hydrodynamic model

By considering a hot gas or plasma as a continuous, compressible medium, we based as in our previous investigations on the following equations for conservation of mass, pulse, and total energy:

$$\begin{aligned}
&\frac{\partial \rho}{\partial t} + \nabla \cdot (\rho \mathbf{v}) = 0, \\
&\frac{\partial}{\partial t} \rho \mathbf{v} + \nabla \cdot (\rho \mathbf{v}\mathbf{v} + p_h) = \mathbf{F}_{ex}, \\
&\frac{\partial e_h}{\partial t} + \nabla \cdot [\mathbf{v}(e_h + p_h)] = \mathbf{v} \cdot \mathbf{F}_{ex}.
\end{aligned} \tag{1}$$

where, ρ - density of plasma, $\mathbf{v}$ - velocity of plasma, p_h - hydrodynamic pressure, and $e_h = \frac{\rho v^2}{2} + e_{\text{int}}$ - sum of kinetic and internal energy densities of plasma. The equation set (1) describes convective motion of a compressible homogeneous medium. To describe the physical processes presented in LPP+DPP system, additional external forces $\mathbf{F}_{ex}$ and sources should be added, and dissipative terms should be taken into account. Here and below, all physical expressions and all transformation use Gaussian units, unless stated otherwise.

In laboratory LPP+DPP experiments, any electromagnetic sources can have an external influence on the plasma, and electric currents can be generated spontaneously by intensive heating of local plasma areas. Any current can be the source of a magnetic field in the plasma, and this magnetic field is the source of forces that disturb the initial plasma. This self-consistent process was included in the hydrodynamic equation set (1). Also, the conservative form of the set was not changed. For this reason, it was introduced an additional conservative variable: magnetic field **B**. An additional equation for the introduced variable should be written and the corresponding forces added into the equation set (1.1). The HEIGHTS general equation set does not operate with currents directly because of the conservative form of the initial equation. In the general case of magnetohydrodynamics, external forces can be expressed as forces that act on the unit charge, such as force field strength $\mathbf{E}$. It may be given as the sum of three forces: Lorenz, electrical field, and Hall force:

$$\mathbf{E} = -\frac{1}{c}\mathbf{v}\times\mathbf{B} + \eta\mathbf{j} + \frac{h_c}{\rho}\mathbf{j}\times\mathbf{B}. \tag{2}$$

To simplify the equation, we transformed the vector form of (1) to the component tensor form in the Cartesian coordinate system. Below we present the final expressions for the considered cases in our paper: 3D Cartesian for laser beams – solid target interaction, and 2D cylindrical for the discharge stage of the hybrid device operational cycle. Numerical simulations of the LPP device with various targets showed very small dependence of the plasma parameters from the thermomagnetic source for laser-radiation power density up to $6.0\cdot10^{11}$ *W/cm*^{2} [14]. Correspondingly, the MHD code can be streamlined this part for more efficient simulation by neglecting the magnetic field and rank reduction of the operating matrixes. General equations system (1) can be presented for this case in form

$$\begin{aligned}
&\frac{\partial\rho}{\partial t}+\frac{\partial\rho v_x}{\partial x}+\frac{\partial\rho v_y}{\partial y}+\frac{\partial\rho v_z}{\partial z}=0,\\
&\frac{\partial\rho v_x}{\partial t}+\frac{\partial}{\partial x}\left(\rho v_x^2+p_t\right)+\frac{\partial\rho v_x v_y}{\partial y}+\frac{\partial\rho v_x v_z}{\partial z}=0,\\
&\frac{\partial\rho v_y}{\partial t}+\frac{\partial\rho v_y v_x}{\partial x}+\frac{\partial}{\partial y}\left(\rho v_y^2+p_t\right)+\frac{\partial\rho v_y v_z}{\partial z}=0,\\
&\frac{\partial\rho v_z}{\partial t}+\frac{\partial\rho v_z v_x}{\partial x}+\frac{\partial\rho v_z v_y}{\partial y}+\frac{\partial}{\partial z}\left(\rho v_z^2+p_t\right)=0,\\
&\frac{\partial e_t}{\partial t}+\frac{\partial}{\partial x}\left(v_x[e_t+p_t]\right)+\frac{\partial}{\partial y}\left(v_y[e_t+p_t]\right)+\frac{\partial}{\partial z}\left(v_z[e_t+p_t]\right)=Q_{i,th}+Q_{e,th}+Q_{las}+Q_{rad},\\
&\frac{\partial e_i}{\partial t}+\frac{\partial}{\partial x}\left(v_x[e_e+p_e]\right)+\frac{\partial}{\partial y}\left(v_y[e_e+p_e]\right)+\frac{\partial}{\partial z}\left(v_z[e_e+p_e]\right)=Q_{e,th}+Q_{ei}.
\end{aligned} \tag{3a}$$

Here $e_t = e_i^{int} + \left(e_e^{int} + I\right) + e_{kin}$ is total energy; $e_e = e_e^{int}$ is electron energy; $p_t = p_e + p_i$ is total pressure; $Q_{e,th}$ is heat conduction of electrons; $Q_{i,th}$ is heat conduction of ions; Q_{las} is laser heat; Q_{rad} is radiation transport; and Q_{ei} is electron-ion interaction. MHD equations for the DPP stage application are expressed for the case of Z-pinch: it is assumed that the plasma current is strongly parallel to the *z*-axis and one is uniform along the φ-axis. At the same time, the current can have a gradient in the *r* and *z* directions. The magnetic field has only one φ-projection in this ideal

symmetric case. This idealization does not exclude general plasma processes. Hence, we can have the *z*-gradient of the magnetic field B_φ as a result of the current *z*-gradient (for example, by fluctuation of resistivity η). In this case, we have the *z*-gradient of magnetic tension $-\frac{B_\varphi^2}{4\pi\mu r}$ and a Rayleigh-Taylor type instability. On the basis of these assumptions, the final MHD system for Z-pinch symmetry that is used in HEIGHTS is given by

$$
\begin{aligned}
&\frac{\partial \rho}{\partial t}+\frac{1}{r}\frac{\partial}{\partial r}\left(r\rho v_r\right)+\frac{\partial}{\partial z}\left(\rho v_z\right)=0,\\
&\frac{\partial \rho v^r}{\partial t}+\frac{1}{r}\frac{\partial}{\partial r}r\left(\rho v_r v_r\right)+\frac{\partial}{\partial z}\left(\rho v_r v_z\right)+\frac{\partial p_{tot}}{\partial r}=-\frac{B_\varphi^2}{4\pi\mu r},\\
&\frac{\partial \rho v_z}{\partial t}+\frac{1}{r}\frac{\partial}{\partial r}r\left(\rho v_z v_r\right)+\frac{\partial}{\partial z}\left(\rho v_z v_z+p_{tot}\right)=0,\\
&\frac{\partial e_{tot}}{\partial t}+\frac{1}{r}\frac{\partial}{\partial r}\left\{r\left[v_r\left(e_{tot}+p_{tot}\right)\right]\right\}+\frac{\partial}{\partial z}\left\{v_z\left[e_{tot}+p_{tot}\right]\right\}=Q_J+Q_{rad}+Q_{th},\\
&\frac{\partial B_\varphi}{\partial t}+\frac{\partial}{\partial r}\left(v_r B_\varphi\right)+\frac{\partial}{\partial z}\left(v_z B_\varphi\right)=Q_{md},
\end{aligned}
\tag{3b}
$$

where $e_{tot}=e_t+e_m=e_t+\frac{B_\varphi^2}{8\pi\mu}$ is total hydrodynamic and magnetic energy; $p_{tot}=p_t+p_m=p_t+\frac{B_\varphi^2}{8\pi\mu}$ is total hydrodynamic and magnetic pressure; Q_J is Joule heating; and Q_{md} is magnetic diffusion. Eqs. (3ab) are closed with the thermodynamic gas properties for corresponding matter: $p=f\left(\rho,e_t\right)$. Because HEIGHTS model included simulation of solid target heat and vaporization, the thermodynamic properties are stored in tables for two cases: solid and gaseous matter. The vaporized material enters to the hydrodynamic domain from the solid target computation domain. As shown, Eqs. (3ab) contains non-convective terms *Q* that affect hyperbolic structure of whole system. Because of calculation efficiency, we used splitting methods in our numerical algorithm to separate the hyperbolic and parabolic parts [16], [17]. As a result, the general solution algorithm has two stages: convective and dissipative. The convective part of initial sets of equations is given in matrix form

$$
\frac{\partial \mathbf{U}}{\partial t}+\frac{\partial \mathbf{F}\left(\mathbf{U}\right)}{\partial x}+\frac{\partial \mathbf{G}\left(\mathbf{U}\right)}{\partial y}+\frac{\partial \mathbf{H}\left(\mathbf{U}\right)}{\partial z}=\mathbf{\Omega},
\tag{4a}
$$

$$
\frac{\partial \mathbf{U}}{\partial t}+\frac{1}{r}\frac{\partial}{\partial r}\left[r\mathbf{F}\left(\mathbf{U}\right)\right]+\frac{\partial \mathbf{P}\left(\mathbf{U}\right)}{\partial r}+\frac{\partial \mathbf{G}\left(\mathbf{U}\right)}{\partial z}=\mathbf{\Omega}.
\tag{4b}
$$

The detailed description of the MHD field $\mathbf{U}$, convective fluxes $\mathbf{F}$, $\mathbf{G}$, $\mathbf{H}$, and external source $\mathbf{\Omega}$ can be found in Refs. [13], [15], [18]. The MHD Eqs. (4ab) is the convective part that include parabolicity due to resistive terms like $\frac{\partial}{\partial x_k}\left(\frac{c^2}{16\pi^2\mu^2}\left[\eta\frac{\partial B_k}{\partial x_m}B_m\right]\right)$ in external source term $\mathbf{\Omega}$. When no resistivity is present, the ideal MHD equations are hyperbolic [19], which means that the equations have wave-like solutions that propagate without dissipation. This allows applying the total variation diminishing (TVD) numerical scheme. There are many TVD schemes, however our

choice is second order Lax-Friedrichs algorithm because it does not use a Riemann solver, thus it can be applied to any system of conservation laws without knowledge of the characteristic waves. As we consider explicit algorithm, we can express variation of any parameter $\mathbf{U}$ in cell i by the flux $\mathbf{F}$ at the cell border as

$$\mathbf{U}_i^{n+1} = \mathbf{U}_i^n + \frac{\Delta t^n}{\mathrm{V}_i} \sum_q \left[\mathrm{S}_i \cdot \left(\mathbf{F}_{i-1/2}^n - \mathbf{F}_{i+1/2}^n \right) \right], \tag{5}$$

where q corresponds to the dimension direction; S_i is the cell border square; and V_i is cell volume. Here is assumed that during the time step $\Delta t = t^{n+1} - t^n$ the physical parameter $\mathbf{U}$ can be transported between neighbor cells only. This is the expression of Courant-Levi limitation on the time step. Main problem of all explicit algorithms is determination of the border fluxes $\mathbf{F}$. Below we present expressions for the calculation of the right border flux $\mathbf{F}_{i+1/2}$ according to the Lax-Friedrichs formulation. To avoid doubling the calculations, our numerical code uses loops by the borders not by the cells, since the right flux $\mathbf{F}_{i+1/2}$ of i-cell is the left flux $\mathbf{F}_{(i+1)-1/2}$ of the neighbor $(i+1)$-cell. We assumed here structured non-equidistant discretization, where the subscript i refers to a quantity located on the cell center, and the subscript $i+1/2$ refers to a quantity located on the cell border. Basic assumption of the Lax-Friedrichs (LF) approach is linear dependence of the border flux from the maximum propagation speed of information at the cell border and the field values in neighbor cells [19]

$$\mathbf{F}_{i+1/2} = f\left(c_{i+1/2}^{\max}, \Delta \mathbf{U}_{i+1/2} \right), \tag{6}$$

Three different waves exist in ideal MHD: slow, Alfven, and fast waves. Following this, the maximum propagation speed of information can be expressed as

$$c_q^{\max} = \left| V_q \right| + \frac{1}{\sqrt{2}} \sqrt{ V_{ac}^2 + \frac{\mathbf{B}^2}{4\pi\mu\rho} + \sqrt{ \left(V_{ac}^2 + \frac{\mathbf{B}^2}{4\pi\mu\rho} \right)^2 - 4\left(V_{ac} V_q^{Alf} \right)^2 } } \quad , \tag{7}$$

where Alfven velocity in direction q is

$$V_q^{Alf} = \frac{\left| B_q \right|}{\sqrt{4\pi\mu\rho}} . \tag{8}$$

Thus, the MHD equations are solved as a decoupled set of hyperbolic and parabolic parts. At each time step the MHD problem is split into decoupled subproblems (which may involve different meshes and solution methods) corresponding to the different physical processes (e.g. plasma flow, transport, diffusion, reactions, etc.) that occur within the computational domain or in individual regions. The various processes are treated sequentially and MHD physics updated after each separate contribution. The splitting error consists of a physical splitting error that would exist even if the

subproblems were to be solved exactly (indicative of the way that subproblems are linked), and a numerical splitting error, related to approximating each subproblem.

2.2 Plasma heat conduction and magnetic diffusion

Following the splitting method, the additional dissipative source-terms are calculated separately with the second (dissipative) stage of the HEIGHTS solver and are used as correctors of the main TVD-LF solution of Eq. (4). One of the most expensive computation part of the full MHD problem is modeling heat conduction and magnetic diffusion in plasma. Using explicit algorithms is non-effectively due to very small time steps. Fully implicit algorithms follow to necessity of large amount of memory and to poor scalability in code parallel versions. In our publications [17], [20], we proposed to use sparse matrix solvers to exclude zero elements from the main solution domain and to reduce cardinally memory allocation. Following this idea, the heat conduction equation

$$\frac{\partial e}{\partial t} - \nabla \lambda \nabla T = 0 \tag{9}$$

and magnetic diffusion equation

$$\frac{\partial \mathbf{B}}{\partial t} + \frac{c^2}{4\pi\mu} \nabla \times \left(\eta \nabla \times \mathbf{B} \right) = 0 \tag{10}$$

can be presented after time and space discretization as the following linear equations set

$$\mathbf{A} \cdot \mathbf{X} = \mathbf{D}. \tag{11}$$

Here in Eqs. (9)-(11), λ is heat conductivity, $\mathbf{X}$ is solution vector (it presents temperature field for the Eq. (9) and magnetic field for Eq.(10)), $\mathbf{A}$ and $\mathbf{D}$ are linear coefficients that depends on plasma properties and boundary and initial conditions [17], [20]. Equation (11) is a closed system, where the number of unknown values equals the number of linear equations if the boundary conditions are determined. In general, boundary conditions on any border Γ are given by $\alpha \lambda \nabla T\big|_\Gamma + \beta T\big|_\Gamma = f\left(T\big|_\Gamma, t\right)$, where the numerical parameters α and β specify the situation at the Γ border for a given heat flux (α = 1, β = 1), given temperature (α = 0, β = 1), or heat flux as a function of temperature. The simplest case of thermally isolated borders can be realized as equivalences $\left.\frac{\partial T}{\partial x}\right|_{\Gamma(x=const)} = 0$, $\left.\frac{\partial T}{\partial y}\right|_{\Gamma(y=const)} = 0$, and $\left.\frac{\partial T}{\partial z}\right|_{\Gamma(z=const)} = 0$. Conditions on the external borders of the domain are determined by various physical processes. Most useful are the following: current $B\big|_\Gamma = 2I/rc$; symmetry $\left.\frac{\partial rB}{\partial r}\right|_{\Gamma(r=const)} = 0$, $\left.\frac{\partial B}{\partial z}\right|_{\Gamma(z=const)} = 0$; and conducting wall $B\big|_\Gamma = 0$. A more comprehensive discussion of boundary conditions is presented elsewhere [21]. Numerical simulation with the implicit scheme is unconditionally stable, and in combined schemes the limiting factor on

the time step is usually the explicit part (the convection stage in our case). In 3D LPP problem, the largest grid size that we had was 60 × 60 × 60 cells, which produces a coefficient matrix of about $1.0 \cdot 10^{16}$ elements. This large sparse matrix has an extremely large number of zero elements. The structure of the matrix is invariable, with linear equations that describe nonuseful cells. Key to computational efficiency is to store and operate on only nonzero entries of the matrix. Several mathematical libraries (e.g., NAG, IMSL, and PARDISO) are used for solution of linear equation systems with a band or sparse matrix. MUMPS and SuperLU codes allow parallel solution of the system of linear equations given in Eq. (11) [22]. Calculations for the complex domain need special code for implementation of boundary conditions and exclusion of nonuseful domain areas

During each time step the implicit scheme drives small scale changes of the temperature or magnetic field to equilibrium states satisfying Eqs. (9) and (10) with the left-hand side set to zero. This time step is viewed as the ‘‘relaxation time’’ to the steady state. At a given time step the resulting equations are elliptic or Poisson's equations for T and B. Space variables are discretized just as in steady state heat and magnetic field diffusion problems. The solution from the previous time step provides an initial guess for the new one. Thus, for the large time steps allowed in the fully implicit scheme, the parabolic equations (9) and (10) can be reduced to the solution of elliptic equations for each time step of the time-space. The main advantage of the fully implicit scheme is that we have accurate error control in the time step selection process allowing step sizes to automatically adjust to the problem physics while maintaining accuracy. The dissipative stage fields $\Delta e_{i,j} = \rho_{i,j} c_{p\{i,j\}} \left(T_{i,j}^{n+1} - T_{i,j}^{n} \right)$ and $\Delta B_{i,j} = B_{i,j}^{n+1} - B_{i,j}^{n}$ can be considered as dissipative sources for the ideal MHD solution at each time step. We utilize these as additional dissipative sources in vector $\mathbf{\Omega}$ on the right side of Eq. (4ab).

2.3 Heat conduction and vaporization in target

Because the time processes of plasma heat conduction are much faster in comparison to the processes in solid or liquid matter no reason to apply complex implicit schemes to simulation of the thermal conductivity and vaporization in the target body. The time step which limited plasma magnetic hydrodynamic processes is very small and allow to avoid numerical oscillation by modeling of the heat conduction in the solid or liquid target with the explicit scheme. The scheme which is applied in HEIGHTS for solid is presented with divergent recalculation similar to the last stage of the plasma heat conduction scheme (divergent recalculation of Eq.(9))

$$e_{i,k}^{n+1} = e_{i,k}^{n} - \frac{\Delta t^n}{r_i \Delta r_i} \left(r_{i+1/2} F_{i+1/2,k}^{n+1} - r_{i-1/2} F_{i-1/2,k}^{n+1} \right) - \frac{\Delta t^n}{\Delta z_k} \left(G_{i,k+1/2}^{n+1} - G_{i,k-1/2}^{n+1} \right), \tag{12}$$

where fluxes F and G are calculated by simple explicit algorithm [23].

Most modern numerical algorithms use mesh reconstruction method for modeling the target vaporization processes. Usually two main approaches are applied: the declaration of the vaporizing cells as special cells with variable size (other cells are constant excluding direct neighbors), and full redesign of mesh at each time step. The first algorithm obtains the unstructured mesh properties, and the second algorithm can be unstructured only in multi-dimensional case. Both ways add significant complication of numerical calculations. We constructed and analyzed algorithm where vaporizing cells have not variable size but have variable artificial density, i.e. amount of matter encased in constant cell. Physical density of vaporizing cell is conserved to be the density of boiling matter. As a result we can calculate the real physical volume of the cell matter (that is smaller than the mesh cell volume after the part of matter is vaporized);

$$V_p = \frac{\rho_a}{\rho_p} V_{cell}, \tag{13}$$

where V_p is physical volume of matter in cell; ρ_p is physical density of boiling matter; ρ_a is artificial density; and V_{cell} is volume of the constant mesh cell. To simulate the energy deposition in cell, we used the real physical properties of vaporizing matter in cell for laser absorption and plasma impact. These algorithms did not change much: laser absorption take place on the surface of liquid (conserved) and the total amount of the scattering centers (conserved) is important for the plasma impact. The surface gas hydrodynamic processes located above the target are shifted on the thickness of vaporized to this moment layer and can be replaced after end of calculation. The vaporization modeling algorithm consists in the mass transfer from the initial cell (which has vaporization temperature) into neighbor gaseous cell each time step. Amount of the transferred vapor is determined by the deposited energy into cell during the time step and the latent heat of vaporization [24], [25].

More essential changes were done for the heat conduction scheme. To conserve physical mechanism of the thermal conductivity, the real physical interfaces between cells (including vaporizing) should be considered. Figure 2 presents the situation between two vaporizing cells.

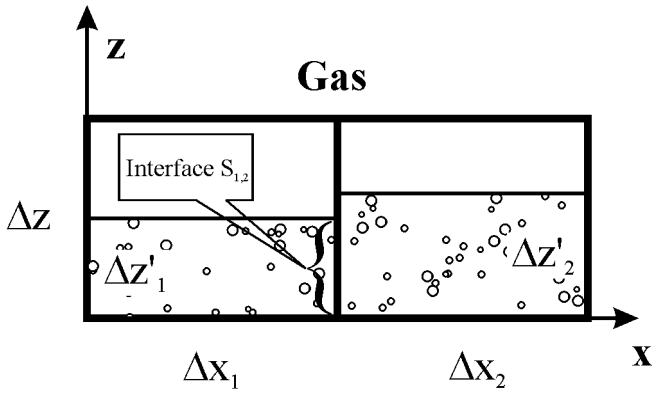

Fig. 2. Physical interface $S_{1,2}$ between vaporizing cells.

The real physical interface is shown in Fig.2. The energy transfer for this condition can be described in finite volume terms as

$$e_1^{n+1} = e_1^n - \Delta t \frac{\min\left(\rho_{a\{1\}}, \rho_{a\{2\}}\right)}{\rho_p} \frac{\mathbf{F}_{1,2}\, S_{1,2}}{V_{cell\{1\}}}, \tag{14}$$

where $\mathbf{F}_{1,2}$ is the heat flux on the (1-2) cells border; $S_{1,2}$ is the mesh interface square between 1st and 2nd cells; $V_{cell\{1\}}$ is the volume of the 1-th cell. The coefficient $\frac{\min\left(\rho_{a\{1\}}, \rho_{a\{2\}}\right)}{\rho_p}$ describes decreasing of contact surface between the 1st and 2nd cells. After the cell is fully vaporized, it is excluded from the target template and included into MHD domain.

2.4 Monte Carlo radiation transport and laser heating

The Monte Carlo method is used for modeling the LPP + DPP radiation processes: laser heating, photon radiation transport in the plasma, and the EUV output. With regard to radiation transport, radiation fluxes should be determined to solve two main problems: 1) correction of the plasma thermal energy and, as a result, correction of the plasma motion in

the device, and 2) determination of the final useful part of the radiation flux (i.e., EUV output). These problems determine the different requirements for the flux data and the numerical techniques needed to solve the photon transport problem. Correct calculation of the energy-space redistribution in full spectrum of the plasma plays an important role in solving the first problem. The constructed model describes radiation transport adequately only if it takes into account the optical thickness of the plasma in a large number of spectral groups. The full spectrum of the LPP plasma is divided into narrow spectral groups with separation of the strongest lines. The total number of the spectral groups was optimized to accurately describe the radiation energy redistribution for a reasonable computational power. As previous calculations show [26], the MHD results have an acceptable error for total spectral groups of about ~10^3. However, such number of groups is unacceptable for investigations in the EUV band of interest, 2% at 13.5 nm. For this reason, we use two sets of optical opacities: general (for full-energy redistribution calculations) and specific (for calculations in the interesting spectral band). The main hydrodynamic simulations use general opacity tables and calculate the evolution of the plasma temperature and density. The final EUV simulations use the detailed opacities to estimate the total device conversion efficiency.

The Monte Carlo algorithm of radiation transport models contains three elementary processes: the emission, motion, and absorption of separate photons. This approach has the advantage of considering complex geometries within the computational domain. The radiation transport model is three dimensional; that is, the photon motion is considered in a 3D Cartesian coordinate system. The cylindrical case involves the accumulation of statistical events in the 2D system of the LPP+DPP device. Studying the trajectory, as well as the number of emitted and absorbed energy at each point of the plasma domain (or the points of major interest), one can calculate the redistribution of energy due to photon transport. Because simulation of all photons in the domain is problematic (computation power is limited), each energy portion is assumed to be a monochromatic set of photons. Hence, a macro-photon has the properties (absorption and emission probabilities) of the component photons, and the energy is equal to the sum of the energies of all photons in the set. To optimize the algorithm and decrease computation time, we introduced a system of weight factors into the Monte Carlo radiation transport model. Two major weight factors were allocated: normalization of the emitted macro-photon relative to the most radiated cell of the computational domain and normalization relative to the optical thickness of cell. The first weight factor is obtained from the emission process analysis and accelerated calculations due to the neglect of the emission of cold cells. Because of the second weight factor, so-called idle processes are ignored, namely, situations involving the emission and the absorption of the photon in the same cell (absorbed lines). A third weight factor can be useful for a strongly nonuniform mesh. The volume of the emitting cell can be so small that the amount needed for simulating photon bundles will not be sufficient to obtain accurate results. The volume weight coefficient should increase the computation accuracy in this case. To complete the simulation of the absorption process in the plasma, we use the absorption coefficient (which depends on matter parameters in the computational domain cell and on photon energy) and the photon path length in this cell. The emission and absorption coefficients calculation in plasma is described in details in Ref. [27].

The laser beam is modeled as a directional flux of macro-photons in analogy to the above Monte Carlo theory for the plasma radiation transport. The separate macro-photon has the same properties (absorption, reflection probability, etc.) as the real laser radiation photon. The total sum of real photons W_{macro} in one macro-photon is estimated from the required accuracy and available computational power:

$$N_{macro} = \frac{N_{real}}{W_{macro}}, \quad N_{real} = \frac{P_{las}}{E_{ph}}, \tag{15}$$

where, P_{las} is the momentary laser power and E_{ph} is the energy of a real laser radiation photon. The inverse bremsstrahlung is assumed to be the main process by which the laser radiation was absorbed by the plasma electrons. The classical value for the absorption coefficient k_{abs}^{las} that defines this collisional absorption mechanism is given by [28]

$$k_{abs}^{las} = \frac{16\pi Z n_e^2 e^6 \ln\Lambda(\nu)}{3c\nu^2 (2\pi m_e k_B T_e)^{3/2} \left(1 - \nu_p^2/\nu^2\right)^{1/2}}, \tag{16}$$

where again e, n_e, m_e, T_e are the electron charge, density, mass, and temperature, respectively; Z is the normalized ionic charge; ν is the frequency of laser light; $\nu_p = \sqrt{\frac{n_e e^2}{\pi m_e}}$ is plasma frequency; and k_B is the Boltzmann constant. The Coulomb logarithm is given by [29]

$$\ln\Lambda = \ln\left[\frac{3}{2}\sqrt{\frac{(k_B T_e)^3}{\pi n_e}}\,\frac{1}{Ze^3}\right]. \tag{17}$$

The laser radiation absorption coefficients in the liquid target and in vapor are obtained from the experimental data [30], [31]. As it shown in Ref. [32], one of the main features of the collision-induced absorption is a quadratic dependence of the absorption coefficient on the density (for our case this corresponds to the pair collisions) and a weak dependence on the temperature [33]. Based on this theory, the absorption coefficient for the target vapor up to 0.7 eV can be obtained by the fitting of the dependence between experimental data for the liquid target [30], [31] and Eq. (16):

$$k_{abs}^{las} \sim \rho^2 T^{1/2}. \tag{18}$$

3. VALIDATION AND BENCHMARKS

The physical and mathematical model assembled for benchmarking included all the blocks described in this report: TVD-LF hydrodynamics, implicit three-diagonal matrix solution for parabolic terms, Monte Carlo radiation transport, Monte Carlo laser absorption, target heat and vaporization processes, and Monte Carlo modeling of EUV output registration. The model was tested with two and three dimension numerical schemes, with similar results. Also were tested several variants of spatial meshes: for 2D 100×250 cells with minimal size of cell in region of interest ~1μm and 65×110 with size ~5μm; for 3D 40×40×45 cells with cell size ~10μm for big spot sizes only. A final parameter that also served as a criterion for the code benchmarking was the total EUV output into 2π sr solid angle, that is, the CE of the LPP device [12]:

$$c_{EUV} = \frac{Q_{EUV}^{13.4nm \pm 1.1eV}}{Q_{las} \cdot 2.2eV} \cdot 100\%, \tag{19}$$

where $Q_{EUV}^{13.4nm \pm 1.1eV}$ is the amount of EUV radiation energy registered in the 2.2 eV bandwidth centered at 134 Å. The efficiency is normalized to 1 eV. Opacities and atomic data used for radiation transport and EUV calculations are described in detail in Refs. [26] and [27].

Figure 3 presents a comparison of experimental results [34], well-known theoretical data (LASNEX [35]), and results simulated by the HEIGHTS package.

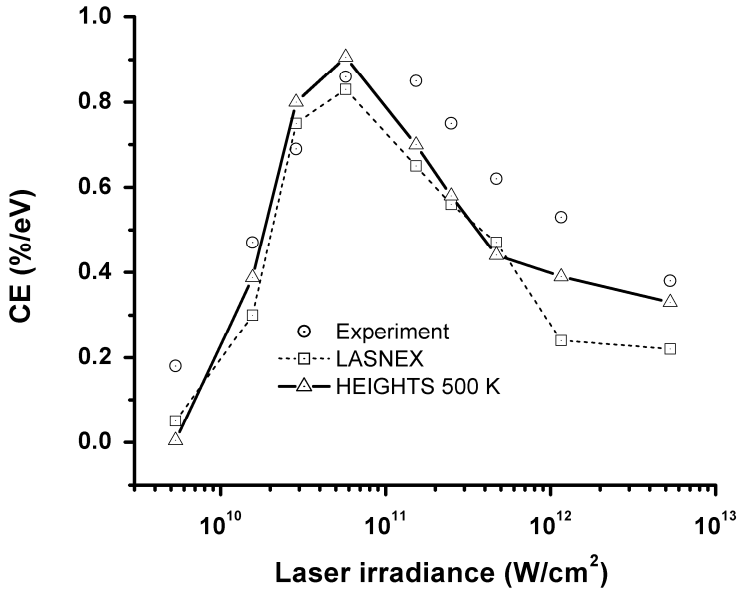

Fig. 3. Efficiency of the LPP device with tin planar target. Comparison of experimental and theoretical data.

To validate our target vaporization model and laser absorption in vapor model, we carried out numerical benchmarking of the experiments described in Ref. [36]. In these experiments, a 2-mm-thick tin target was irradiated with the 1064-nm Nd:YAG laser during 8 ns. Spot radius was 500 μm and laser intensity ~ 2 GW/cm^2. Figure 4 shows a comparison of our calculations with experimental measurements: temperature - time dependence at 1 mm above target surface and space distribution of electron density at the laser beam axis.

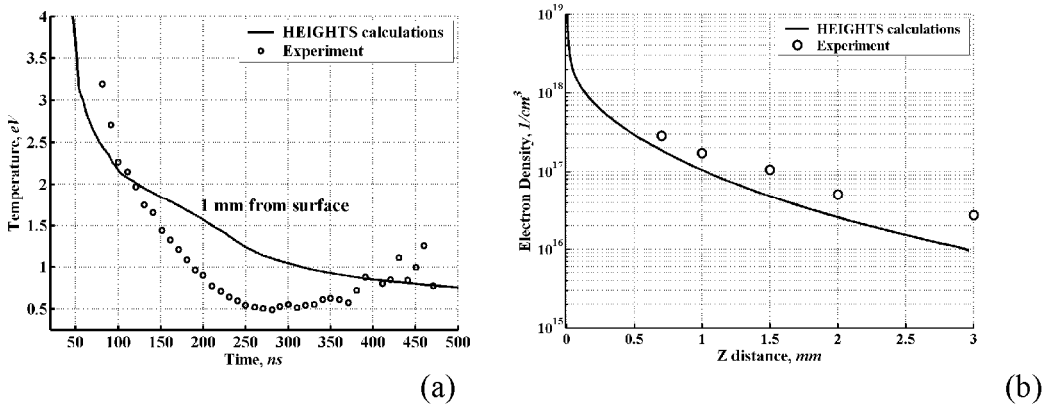

Fig. 4. Comparison of experimental [36] and HEIGHTS modeling data: a) temperature time curve in 1 mm above target surface; b) space distribution of electron density on the laser beam axis.

As shown, the HEIGHTS numerical results agree well with the published data. The numerical scheme demonstrated stability of results with changing the spatial discretization and with expansion to full 3D structure. These results indicate that the full 3D HEIGHTS package can be used effectively to study complex three-dimensional magnetohydrodynamics problems.

5. NUMERICAL RESULTS

In our numerical simulation studies we investigated parameters of laser prepared plasma for the optimal discharge stage performance. The basic device geometry is presented in Fig.1. The cathode-anode distance was ~ 3.6 mm and the anode hole diameter ~5.0 mm. Figure 5 describe intensity time dependence of the laser device. The assumed as variation value initial discharge energy was equal ~ 2.5 J.

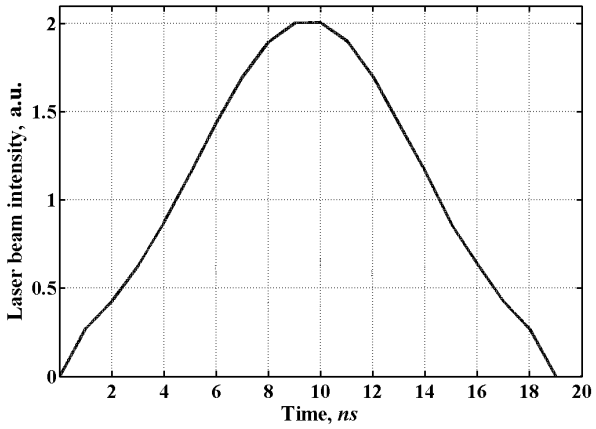

Fig. 5. Gaussian laser pulse form used in simulation of LPP+DPP device.

Laser heating stage of hybrid device should prepare low-temperature homogeneous plasma for an effective start of the discharge and optimum pinching as a result. Presented initial parameters of the LPP+DPP device allowed plasma expansion from cathode to anode during ~ 100 ns after the laser beam impact start. Plasma temperature and composition evolution is shown in Fig. 6 for this time period.

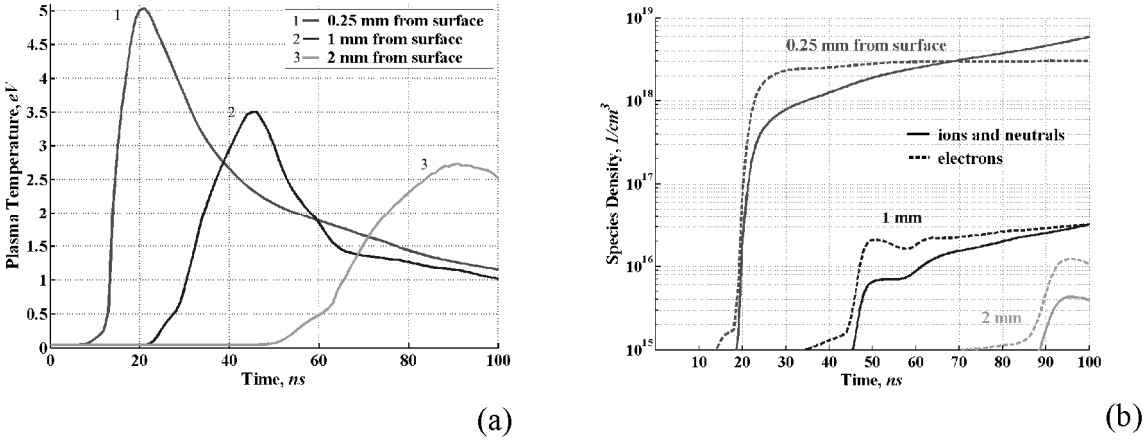

Fig. 6. Plasma temperature (a) and plasma composition (b) evolution above the tin target surface during the LPP stage.

Figure 7 presents typical plasma electron density and temperature directly before the discharge start. As it is shown, prepared plasma distribution is very inhomogeneous. This will have the effect of unstable pinching with z-axis elongate

form. Moreover, some of initial LPP stage parameters bring to the dual pinch form. Dual pinch form is corresponding to the experimental data [37] shown in Fig. 8. HEIGHTS package was able to produce the dual pinch form of these experiments accurately.

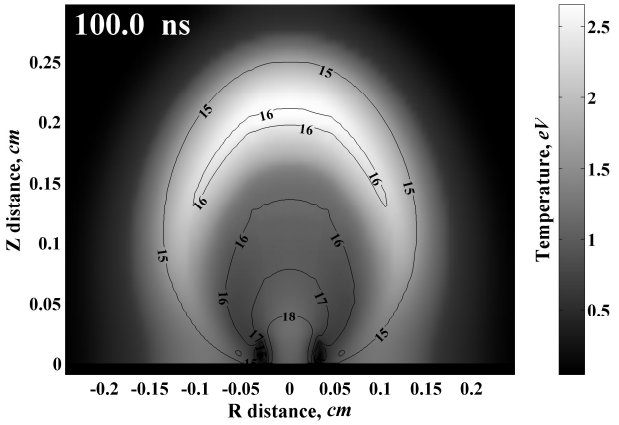

Fig. 7. Plasma electron temperature (eV, palette) and plasma electron density (ln(cm^{-3}), contours).

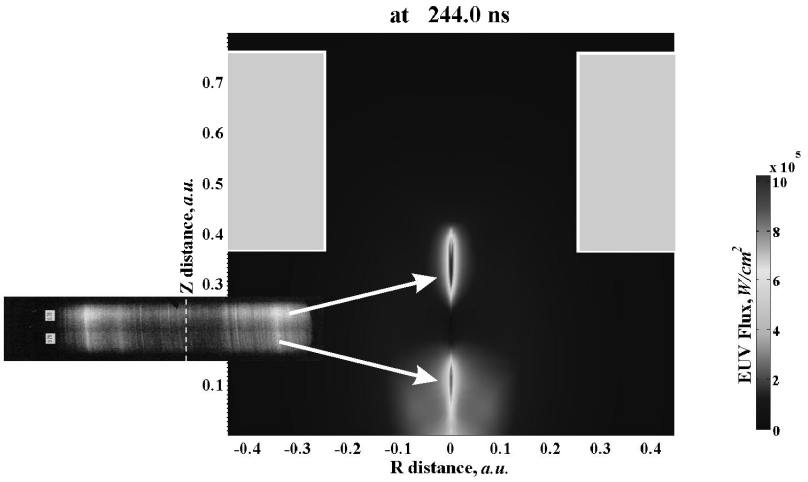

Fig. 8. Dual EUV generation region. Correspondence of the experimental data (spectrometer band at left) [37] and HEIGHTS calculations of EUV field (background picture).

Various LPP+DPP devices geometries were also modeled. Main goal of initial parameters optimization was to obtain homogeneous plasma distribution for the discharge start. Design versions without anode hole were also considered. The obtained numerical data was used to optimize the hybrid device condition, decrease device wall loading, reduce debris emission and construct proper reflection mirror system.

6. CONCLUSIONS

The developed integrated and benchmarked models in HEIGHTS package was applied to simulation and optimization of hybrid DPP and LPP devices and calculation of initial parameters for debris mitigation devices and reflection system. Optimization of various parameters was carried out in a wide range. Optimization of plasma homogeneity after the LPP stage is proposed for improvement of the DPP process. Further investigations of the effect of plasma confinement on the final CE of the hybrid devices should involve optimization of initial parameters: laser beam arrangement in space, laser power density distribution in time and in cross-section of beam, laser pulse duration, target geometry, and target structure.

7. ACKNOWLEDGMENTS

This work was initially supported by the Intel Corporation and SEMATECH.

REFERENCES

[1] Silverman P.J., "The Intel Lithography Roadmap," Intel Tech. J., 3, 55-61 (2002).

[2] Bakshi V., "EUV source technology: challenges and status," in [EUV Sources for Lithography] Bakshi V., Ed., Bellingham, Washington: SPIE. Ch. 1, 3-25 (2006).

[3] Stamm U., "Extreme ultraviolet light sources for use in semiconductor lithography – state of the art and future development," J. Phys. D, 37, 3244-3253 (2004).

[4] Pankert J., Apetz R., Bergmann K., Derra G., Janssen M., Jonkers J., Klein J., Kruecken T., List A., Loeken M., Metzmacher C., Neff W., Probst S., Prummer R., Rosier O., Seiwert S., Siemons G., Vaudrevange D., Wagemann D., Weber A., Zink P., and Zitzen O., "Integrating Philips extreme UV source in the alpha-tools," Proc. SPIE 5751, 260-271 (2005).

[5] Myers D.W., Fomenkov I.V., Hansson B.A.M., Klene B.C., and Brandt D.C., "EUV source system development update: advancing along the path to HVM," Proc. SPIE 5751, 248-259 (2005).

[6] Krücken T., Bergmann K., Juschkin L., and Lebert R., "Fundamentals and limits for the EUV emission of pinch plasma sources for EUV lithography," J. Phys. D, 37, 3213-3224 (2004).

[7] Richardson M., Koay C.-S., Takenoshita K., Keyser C., George S., Teerawattansook S., Al-Rabban M., and Scott H., "Laser plasma EUVL sources: progress and challenges," Proc. SPIE 5374, 447-453 (2004).

[8] Korobkin Yu.V., Romanov I.V., Rupasov A.A., Shikanov A.S., Gupta P.D., Khan R.A., Kumbhare S.R., Moorti A., and Naik P.A., "Hard X-ray emission in laser-induced vacuum discharge," Laser and Particle Beams, 23, 333-336 (2005).

[9] Pankert J., "Philips's EUV Source: Update and Issues," presented on SEMATECH EUV Source Workshop, February 27, San Jose, CA (2005). http://www.sematech.org/meetings/archives/litho/euvl/20050227/pres/06Pankert.pdf

[10] Koshelev K., "Spectroscopic diagnostic of EUV radiating plasmas and optimization of EUVL sources," presented on SEMATECH EUV Source Workshop, February 27, San Jose, CA (2005). http://www.sematech.org/meetings/archives/litho/euvl/20050227/pres/10Koshelev.pdf

[11] Hassanein A., Sizyuk V., Sizyuk T., and Morozov V., "Optimization of EUV laser and discharge devices for high-volume manufacturing," Proceedings of SPIE 6517, 65171X (2007).

[12] Sizyuk V., Hassanein A., and Sizyuk T., "Hollow laser self-confined plasma for extreme ultraviolet lithography and other applications," Laser and Particle Beams, 25(2), 143-154 (2007).

[13] Sizyuk V., Hassanein A., and Sizyuk T., "Three-dimensional simulation of laser-produced plasma for extreme ultraviolet lithography applications," Journal of Applied Physics, 100(10), 103106 (2006).

[14] Sizyuk V., Hassanein A., Morozov V., Tolkach V., and Sizyuk T., "Numerical simulation of laser-produced plasma devices for EUV lithography using the HEIGHTS integrated model," Numerical heat transfer, Part A, 49(3), 215-236 (2006).

[15] Hassanein A., Sizyuk V., Tolkach V., Morozov V., and Rice B.J., "HEIGHTS initial simulation of discharge produced plasma hydrodynamics and radiation transport for extreme ultraviolet lithography," Journal of Microlithography, Microfabrication, and Microsystems, 3(1), 130-138 (2004).

[16] Kovenya V.M., Cherny S.G., and Lebedev A.S., in [Computational Fluid Dynamics], Ed. by Davis G.S. and Fletcher C., North-Holland, Amsterdam (1988).
[17] Miloshevsky G.V., Sizyuk V.A., Partenskii M.B., Hassanein A., and Jordan P.C., "Application of finite-difference methods to membrane-mediated protein interactions and to heat and magnetic field diffusion in plasmas," Journal of Computational Physics, 212, 25-51 (2006).
[18] Hassanein A., Sizyuk V., Tolkach V., Morozov V., and Rice B.J., "HEIGHTS initial simulation of discharge-produced plasma hydrodynamics and radiation transport for EUV lithography," Proceedings of SPIE 5037(2), 714-727 (2003).
[19] Tóth G. and Odstrčil D., "Comparison of some Flux Corrected Transport and Total Variation Diminishing Numerical Schemes for Hydrodynamic and Magnetohydrodynamic Problems," J.Comp.Phys., 128, 82 (1996).
[20] Sizyuk V., Hassanein A., Morozov V., and Sizyuk T., "HEIGHTS Integrated Model as Instrument for Simulation of Hydrodynamic, Radiation Transport, and Heat Conduction Phenomena of Laser-Produced Plasma in EUV Applications," Argonne National Laboratory Report ANL-MCS-CPH-06/56, Argonne, IL (2006).
[21] Roach P. J., [Computational fluid dynamics], Hermosa Publishers, Albuquerque, NM, (1976).
[22] Amestoy P.R., Duff I.S., L'excellent J.-Y., Li X.S., "Analysis and comparison of two general sparse solvers for distributed memory computers," ACM Transactions on Mathematical Software, 27(4), 388-421 (2001).
[23] Samarskii A.A., Vabishchevich P.N., [Computational Heat Transfer], John Wiley & Son Ltd, United Kingdom (1996).
[24] Hassanein A.M., "Simulation of plasma disruption induced melting and vaporization by ion or electron beam," Journal of Nuclear Materials, 122&123, 1453-1458, (1984).
[25] Hassanein A.M., Kulcinski G.L., and Wolfer W.G., "Surface melting and evaporation during disruptions in magnetic fusion reactors," Nuclear Engineering and Design/Fusion, 1(3), 307-324 (1984).
[26] Morozov V., Sizyuk V., Hassanein A., and Tolkach V., "Simulation of discharge produced plasma and EUV radiation in various z-pinch devices," Argonne National Laboratory Report ANL-ET-04/31, Argonne, IL (2004).
[27] Morozov V., Tolkach V., and Hassanein A., "Calculation of tin atomic data and plasma properties," Argonne National Laboratory Report ANL-ET-04/24, Argonne, IL (2004).
[28] Johnston T.W. and Dawson J.M., "Correct values for high-frequency power absorption by inverse bremsstrahlung in plasmas," Physics of Fluids, 16, 722 (1973).
[29] Spitzer L., [Physics of Fully Ionized Gases], 2nd ed., New York: Interscience (1962).
[30] Petrakian J.P., Cathers A.R., Parks J.E., MacRae R.A., Callcott T.A., and Arakawa E.T., "Optical properties of liquid tin between 0.62 and 3.7 eV," Phys. Rev. B, 21(8), 3043-3046 (1980).
[31] Cisneros G., Helman J.S., Wagner C.N.J., "Dielectric function of liquid tin between 250 and 1100 °C," Phys. Rev. B, 25(6), 4248-4251 (1982).
[32] Grigoryan G.G., Leonov A.G., Manykin E.A., Rudenko A.A., Sitnikov M.G., and Starostin A.N., "The near infrared (0.8−2.6μm) absorption spectrum of a dense sodium vapor and possible mechanisms of the spectrum formation," Journal of Experimental and Theoretical Physics, 97(4), 678-687 (2003).
[33] Frommhold L., [Collisional-induced absorption in gases], Cambridge Univ. Press, Cambridge, (1993).
[34] Spitzer R.C., Orzechowski T.J., Phillion D.W., Kauffman R.L., and Cerjan C., "Conversion efficiencies from laser-produced plasmas in the extreme ultraviolet regime," J. Appl. Phys., 79, 2251 (1996).
[35] Zimmerman G.B. and Kruer W.L., "Numerical simulation of laser-initiated fusion," Comm. Plasm. Phys. Cont. Fusion, 2(2), 51 (1975).
[36] Harilal S.S., O'Shay Beau, Tillack S., and Mathew Manoj V. "Spectroscopic characterization of laser-induced tin plasma," J. Appl. Phys. 98, 013306 (2005).
[37] Koshelev K., Bakshi V., "Benchmarking Modeling of DPP EUV Sources." Presentation on EUV Source Workshop, Vancouver, May 25 (2006).